Supporting Information

Rationally Reconstructing Attapulgite to MCM-41 and its Superior Application in Formaldehyde Degradation

Dan Chen[a,b,*], Jing Zhang[a], Ming Zhai[a], Xin Chen[a], Liqi Miao[a], Kan Li[a], Zhong Wang[c], Xiaozhi Wang[a,b,*]

[a] *College of Environmental Science and Engineering, Yangzhou University, Yangzhou 225127, P.R. China*

[b] *School of Chemistry and Chemical Engineering, Yangzhou University, Yangzhou 225002, P.R. China*

[c] *Key Laboratory of Biofuels, Qingdao Institute of Bioenergy and Bioprocess Technology, Chinese Academy of Sciences, Qingdao 266101, P.R. China*

S1 Materials

Tetraethyl orthosilicate (TEOS), hydrochloric acid (HCl), cetyl trimithyl ammonium bromide (CTAB), sodium hydroxide (NaOH) and silver nitrate ($AgNO_3$), all analytical reagent grade, were purchased from Sinopharm Chemical Reagent Co., Ltd. Purified Attapulgite (ATP) was obtained from Jiuchuan Nanomaterials Technology Co., Ltd.

S2 ATP acidification

The acidification of ATP was performed using following procedure. 2.0 g ATP were introduced into 20 mL 1.6 mol·L^{-1} HCl solution and stirred for a duration of 30 min. Subsequently, the resulting mixture was transferred to an autoclave and subjected to heating in an oven at 453 K for 18 h. Upon completion of the thermal

* Corresponding author. Tel.: +86-13665282663
E-mail address: chendan@yzu.edu.cn *(Dan Chen),* xzwang@yzu.edu.cn *(Xiaozhi Wang).*

27 treatment, the autoclave was cooled to room temperature, after which the mixture
28 underwent a constantly continuous filtration and wash with deionized water until the
29 pH of the filtrate approximately approached 7.0. The residue was then dried at 393 K
30 for a period of 4 h and designated as PATP.

31 **S3 MCM-41 construction**

32 2.43 g CTAB were introduced to 60 mL 0.2 mol·L^{-1} NaOH under stirring. Then
33 silicon source (3.36 g ATP, 3.36 g PATP or 12.5 mL TEOS) was added to
34 aforementioned solution, and the mixture was kept stirring for 5 h. Following this, the
35 resulting mixture was transferred to an autoclave and heated to 383 K for 48 h. Once
36 the autoclave had cooled to room temperature, the precipitate was filtered and washed
37 thoroughly with deionized water. The support powder was obtained after an overnight
38 drying process at 373 K, followed by calcination at 823 K for 8 h. These samples
39 were denoted as ATP-MCM-41, PATP-MCM-41 or TEOS-MCM-41 according to the
40 silicon source employed.

41 **S4 $AgNO_3$ impregnation**

42 0.126g $AgNO_3$ was dissolved in a small volume water. Next, 1g MCM-41 (ATP-
43 MCM-41, PATP-MCM-41 or TEOS-MCM-41) was gradually introduced into the
44 $AgNO_3$ solution in three separate aliquots, with continuous stirring. The resulting
45 mixture was then left for stand overnight in a beaker. After drying the aforementioned
46 solution to evaporate water, the residue was grinded to a fine powder. Finally, the
47 catalyst powder collected was named as Ag/ATP-MCM-41, Ag/PATP-MCM-41 and
48 Ag/TEOS-MCM-41 in accordance with MCM-41 used.

49 **S5 Catalyst characterization**

50 The surface morphology was characterized by S-4800II field emission scanning
51 electron microscope (Hitachi, Japan), operated at magnification of x20-x800000 and

52 acceleration voltage of 0.5-30 kV. The resolution of SEM images was 1.0 nm.

53 N_2 adsorption-desorption isotherms were collected from NOVA4200e specific
54 surface area analyzer (Quantachrome, America). Specific surface area (S_{BET}) was
55 computed with Brunauer-Emmett-Teller (BET) method. Pore size distribution (PSD)
56 and total pore volume (V_{total}) was calculated using Non-Local Density Functional
57 Theory (NLDFT) model. Average pore diameter (D_{aver}) was calculated with following
58 formula: $D_{aver} = 4V_{total}/S_{BET}$. Before measurement, the samples were treated by
59 degassing at 300 °C for 4 h.

60 Powder X-ray diffraction (XRD) patterns were recorded on D8 Advance A25
61 polycrystalline X-ray diffractometer (Bruker, Germany) with Cu Kα radiation,
62 operated under tube voltage and current of 40 kV and 200mA. The wide and small
63 scanning angle was relatively 10-80° and 0-10° with scanning step size of 0.02°.

64 ^{29}Si nuclear magnetic resonance (^{29}Si NMR) experiments was carried out on
65 Avance 600 nuclear magnetic resonance spectrometer (Bruker, Germany) with
66 magnetic field strength of 14.1 T and linear resolution of 0.102 nm.

67 The thermogravimetric analysis (TG) was performed on Pyris 1 TGA
68 thermogravimetric analyzer (PerkinElmer, USA) with temperature accuracy lower
69 than ± 0.1 °C.

70 Transmission electron microscopy (TEM) imaging was conducted on Tecnai 12
71 (Philips, Netherlands) at accelerating voltage of 120 kV for visual observation of
72 porosity and Ag nanoparticle distribution. Before measurements, the samples were
73 subject to calcination treatment at 500 °C and suspended in ethanol.

74 Ultraviolet-visible spectroscopy (UV-vis) analysis was carried out on Cary 5000
75 (Varian, America) with wavelength accuracy of ± 0.08 nm (UV/Vis).

76 X-ray photoelectron spectroscopy (XPS) was performed on ESCALAB 250Xi

(Thermo Scientific, America) using monochromatic Al Kα radiation (1486.6 eV). Sample charging effects were compensated for by calibrating all binding energies (BE) with the C 1s peak of adventitious carbon at 284.6 eV.

Inductively coupled plasma atomic emission spectroscopy (ICP-AES) experiment were operated on Optima 7300 DV (Thermo Fisher Scientific, America) to detect the practical Ag loading and the differences of Al, Mg and Fe contents in different samples.

S6 Catalytic activity test

HCHO oxidation activity tests were carried out by a fixed-bed flow reactor at atmospheric pressure using approximately 0.2 g catalyst. Gaseous HCHO was generated by flowing 15 $mL \cdot min^{-1}$ N_2 (99.5%, balanced with Ar) over trioxymethylene (99.5%, Acros organics) in an incubator kept in an ice-water mixture. The aforementioned N_2 flow is later mixed with 35 $mL \cdot min^{-1}$ O_2 (30%, balanced with N_2) flow to simulate air. The flow passing through the reactor in all the experiments were controlled by a mass-flow meter. And the feeding stream consisted of a mixture of 500 ppm HCHO, 20 vol.% oxygen and balanced N_2. The effluents from the reactor were analyzed by GC 7890II on-line gas chromatograph (Techcomp, China) equipped with an FID detector. To determine the exact concentration of produced CO_2, a nickel catalyst converter was placed before the FID detector and used for converting CO_2 quantitatively into methane in the presence of hydrogen. In typically runs, the reaction data were obtained after HCHO oxidation was performed for 1 h in order to assure CO_2 concentration in the effluents was steady. Once CO_2 concentration reach its highest level at a certain temperature, HCHO oxidation was considered as thorough. Thus, HCHO conversion was calculated as follows: HCHO conversion (%) = $[CO_2]_{out}$ / $[CO_2]_{max}$ × 100%, where $[CO_2]_{out}$ is the concentration of CO_2 produced at different

temperatures and $[CO_2]_{max}$ is the highest $[CO_2]_{out}$ when HCHO is considered to be completely oxidized.

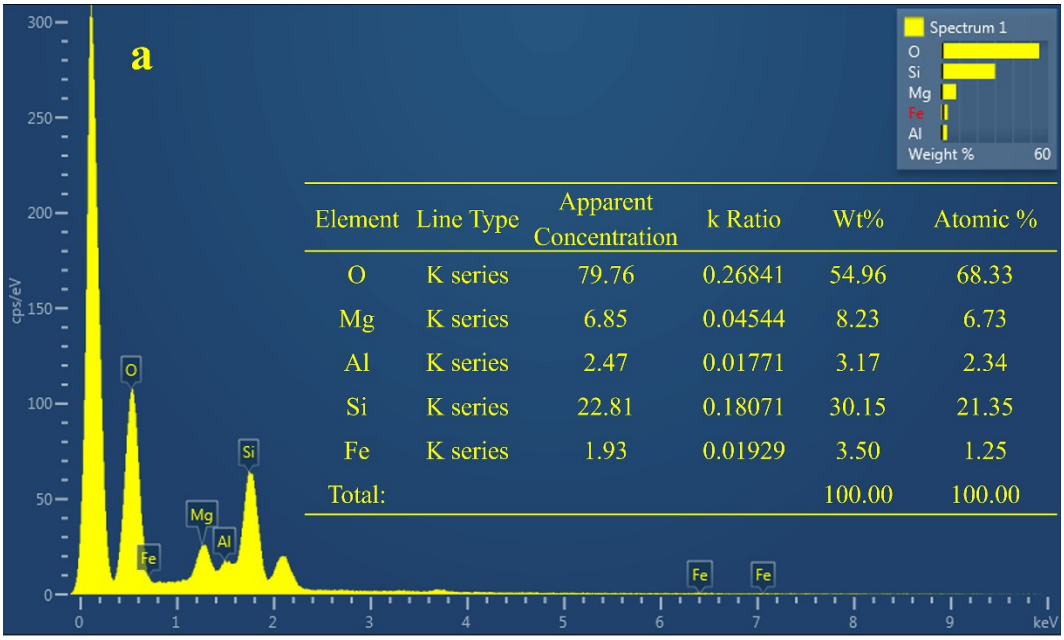

Element	Line Type	Apparent Concentration	k Ratio	Wt%	Atomic %
O	K series	79.76	0.26841	54.96	68.33
Mg	K series	6.85	0.04544	8.23	6.73
Al	K series	2.47	0.01771	3.17	2.34
Si	K series	22.81	0.18071	30.15	21.35
Fe	K series	1.93	0.01929	3.50	1.25
Total:				100.00	100.00

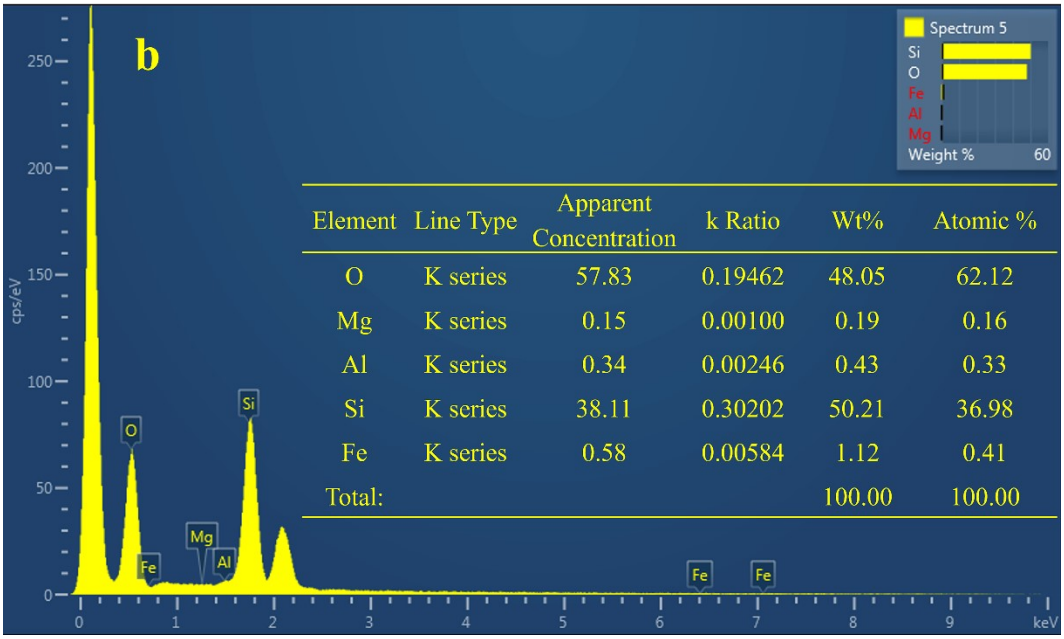

Element	Line Type	Apparent Concentration	k Ratio	Wt%	Atomic %
O	K series	57.83	0.19462	48.05	62.12
Mg	K series	0.15	0.00100	0.19	0.16
Al	K series	0.34	0.00246	0.43	0.33
Si	K series	38.11	0.30202	50.21	36.98
Fe	K series	0.58	0.00584	1.12	0.41
Total:				100.00	100.00

Fig. S1 EDS analysis of element contents for ATP-MCM-41 (a) and PATP-MCM-41 (b), derived from SEM results.

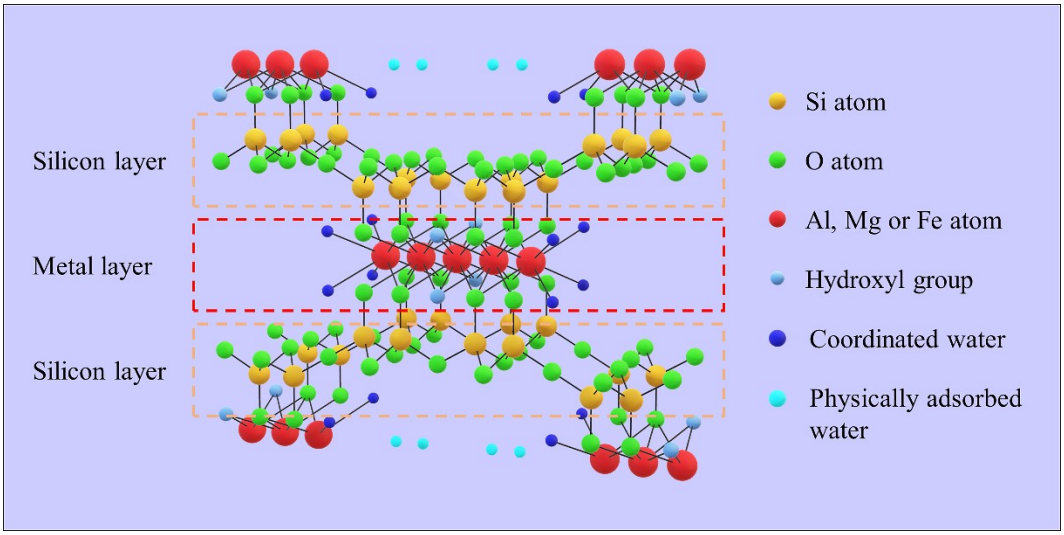

Fig. S2 3D model of sandwich-like attapulgite crystalline structure.

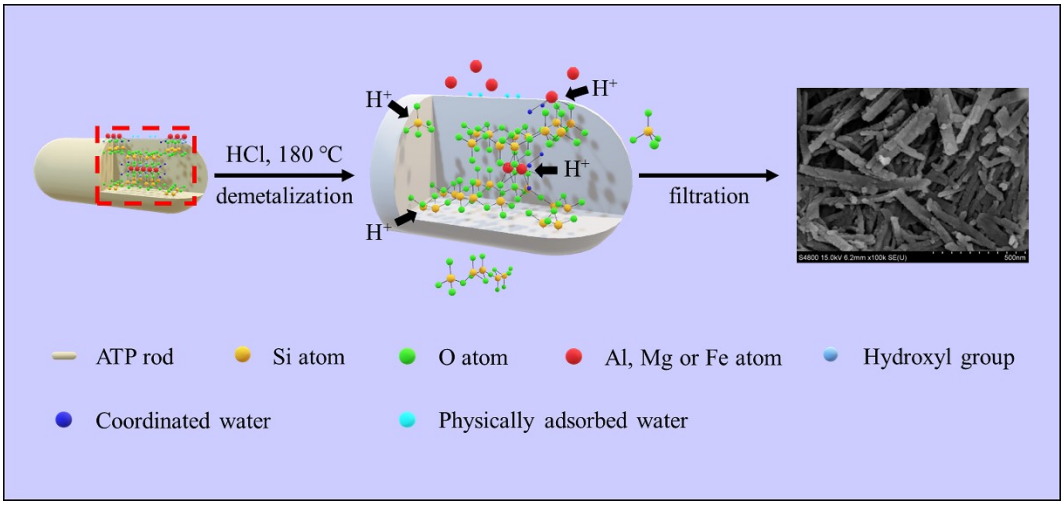

Fig. S3 Schematic illustration of ATP acidification.

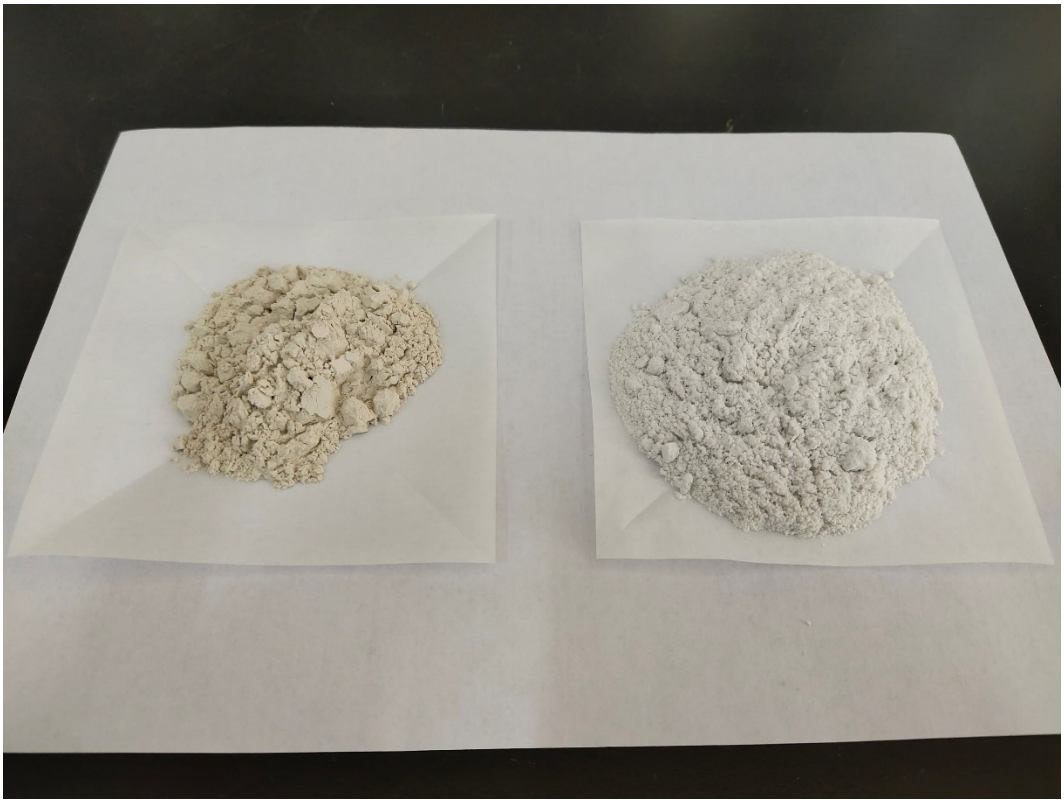

Fig. S4 Comparation of 10 g ATP (left) and 5 g PATP (right) powder.

Total used ATP: M_{ATP} = 18.0032 g.

Total gained PATP: M_{PATP} = 9.2354 g

Weight loss after acidification: W_L (%) = 1-M_{PATP}/M_{ATP}*100% = 48.70 %

Fig. S5 The weight of ATP (a-b) for preparation of PATP and gained PATP (c-f) after acidification.

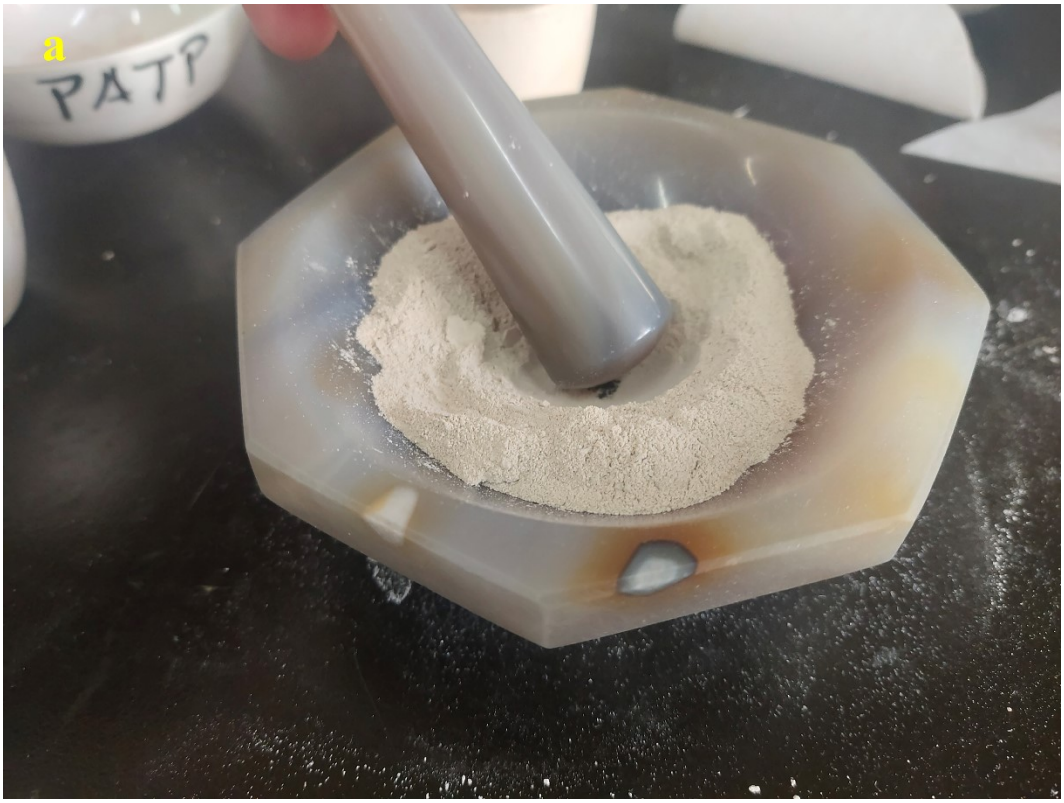

Fig. S6 Macroscopical difference of electrostatic characteristic between ATP (a) and PATP (b).

Fig. S7 Tyndall effect of filtrates gained after hydrothermally treating PATP (left) and ATP (middle) with NaOH, deionized water (right) as contrast.

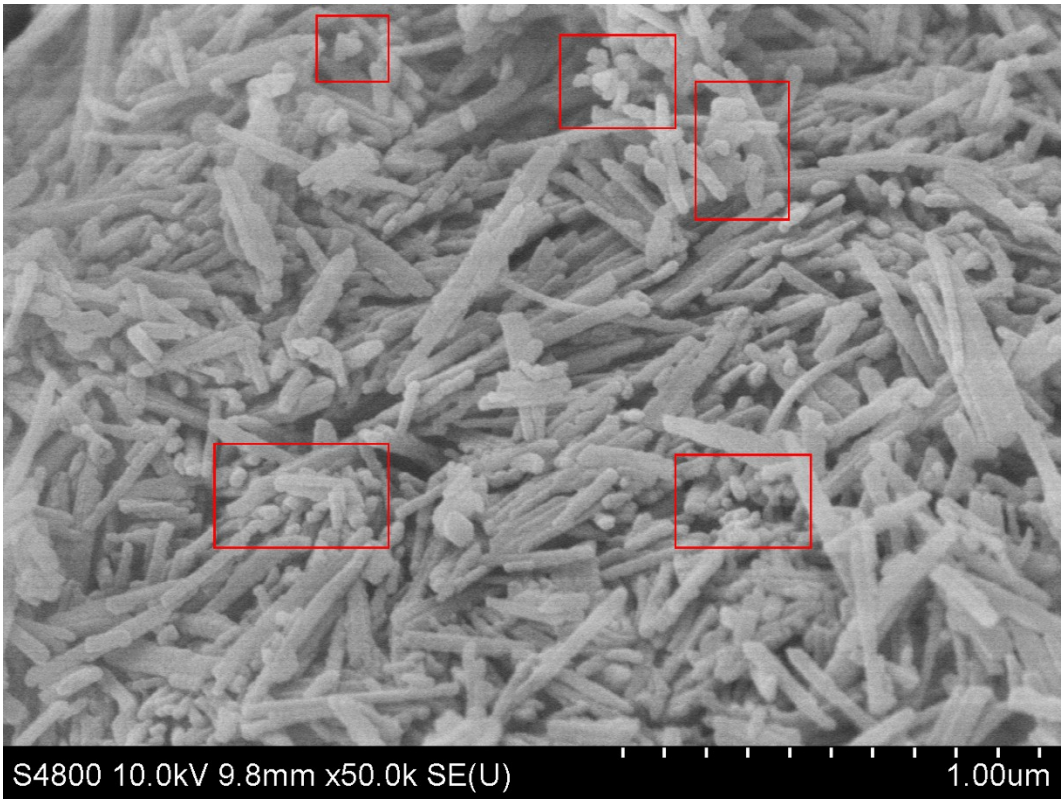

Fig. S8 SEM image of NaOH treated PATP.

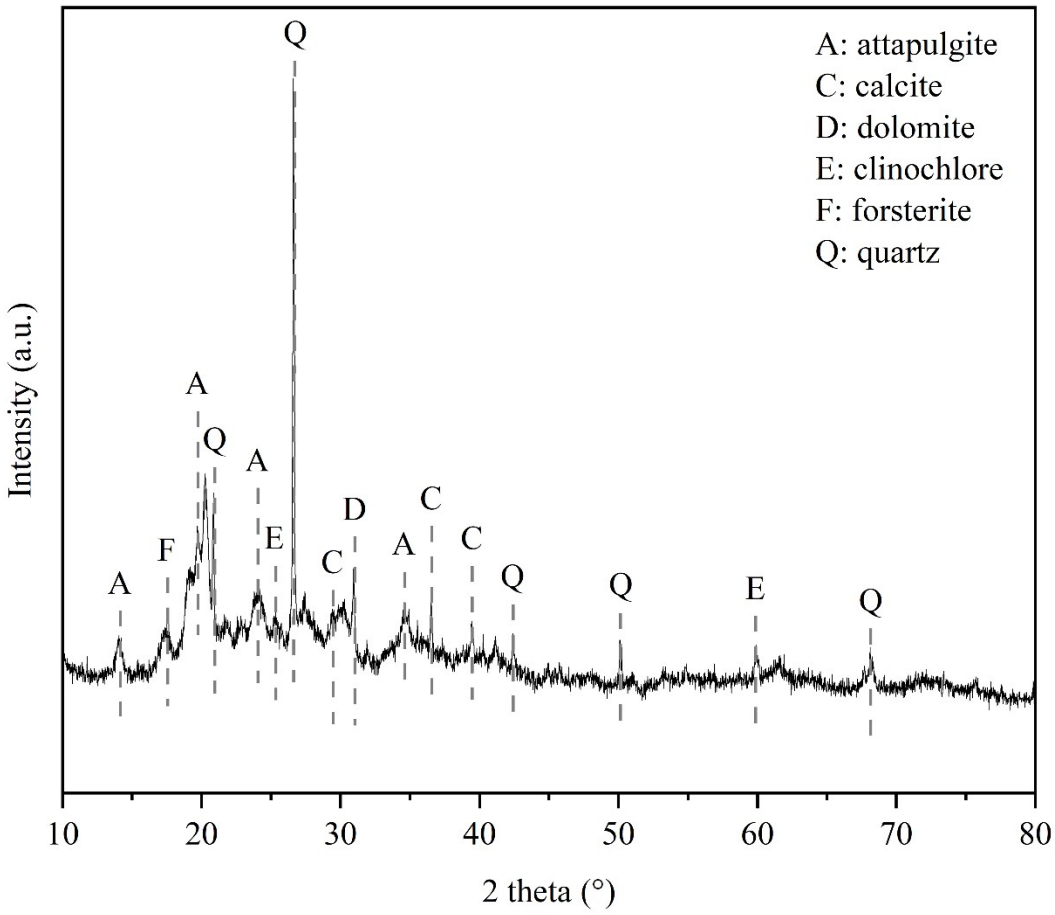

Fig. S9 WXRD pattern of raw ATP.

Table S1 Weight differences of Mg, Al, Fe and Ca element between ATP and PATP, calculated from ICP-AES results.

Sample	Mg (wt%)	Al (wt%)	Fe (wt%)	Ca (wt%)
ATP	4.87	4.48	3.02	1.29
PATP	0.06	0.16	0.15	0.12

Reference

[1] C. Duan, Y. Zhou, M. Meng, H. Huang, H. Ding, Q. Zhang, R. Huang, M. Yan, Research on the Elimination of Low-concentration Formaldehyde by Ag Loaded onto Mn/CeO_2 Catalyst at Room Temperature, Phys. Chem. Chem. Phys. 25 (2023) 24495–24507. https://doi.org/10.1039/D3CP01612A.

[2] B. Huang, Y. Chang, H. Wang, Z. Qu, Synergistic Effects of Acid-metal Dual-site of Ag-Fe/SBA-15 Catalyst Boosting the Elimination of Formaldehyde, Chem. Eng. J. 484 (2024) 149658. https://doi.org/10.1016/j.cej.2024.149658.

[3] S. Lu, N. Sun, N. He, F. Zheng, Y. Jiang, H. Fu, J. Liu, Y. Fang, Mesoporous Ag-K-Al_2O_3 Catalysts Prepared via a One-pot Evaporation Induced Self-assembly Approach and Their Application in Catalytic Oxidation of Formaldehyde, Appl. Surf. Sci. 679 (2025) 161203. https://doi.org/10.1016/j.apsusc.2024.161203.

[4] R. Ousji, Z. Ksibi, A. Ghorbel, C. Fontaine, The Effect of Metal-Support Interactions on Formaldehyde Oxidation and By-Product Selectivities in TiO_2 Supported Metal Catalysts (Co, Cr, Mo, and Ag)., Chem. Africa 6 (2023) 2631–2640. https://doi.org/10.1007/s42250-023-00666-8.

[5] R. Ousji, M.A. Bouabdellah, Z. Ksibi, A. Ghorbel, C. Fontaine, Enhancing Low-Temperature HCHO Oxidation: Investigation selectivity and Catalytic Activity of Ag, Co, Mo, and Cr Catalysts Supported on γ-Al2O3, Chem. Africa 7 (2024) 4005–4015. https://doi.org/10.1007/s42250-024-00967-6.

[6] J. Gong, M. Zhang, J. Li, X. Wang, Y. Zhou, C. Yang, Y. Hua, C. Wang, A. Yuan, Lattice-confined Ag over MnCoLDH Accelerated Catalytic Oxidation of Formaldehyde at Ambient Temperature: The Novel Pathway with Different Oxygen Species, Appl. Surf. Sci. 669 (2024) 160513. https://doi.org/10.1016/j.apsusc.2024.160513.

[7] S. Hu, J. Zhang, X. Chen, X. Qin, J. Yao, C. Zhang, Synergically Regulated Silver Species and Surface Oxygen on Manganese Oxide for Promoted Activity of Formaldehyde Oxidation, J. Environ. Sci. 138 (2024) 709–718. https://doi.org/10.1016/j.jes.2023.05.006.

[8] D. Li, P. Liu, Y. Zheng, Y. Wu, L. Ling, L. Chen, F. Hao, Y. Lv, W. Xiong, H. Luo, Chitosan-promoted Sepiolite Supported Ag as Efficient Catalyst for Catalytic Oxidative Degradation of Formaldehyde at Low Temperature, J. Environ. Chem. Eng. 10 (2022) 108510. https://doi.org/10.1016/j.jece.2022.108510.

[9] S. Lu, C. Su, G. Wang, H. Wang, W. Xia, J. Cui, Q. Zhu, Metal–organic Frameworks Derived Ag/Co_3O_4–MnO_2 for the Catalytic Oxidation of Formaldehyde, React. Kinet. Mech. Catal. 135 (2022) 687–703. https://doi.org/10.1007/s11144-022-02163-4.

[10] X. Chen, H. Wang, M. Chen, X. Qin, H. He, C. Zhang, Co-function Mechanism of Multiple Active Sites over Ag/TiO_2 for Formaldehyde Oxidation, Appl. Catal. B Environ. 282 (2021) 119543. https://doi.org/10.1016/j.apcatb.2020.119543.